

Supporting Information for

A Rational Electrode-Electrolyte Design for Efficient Ammonia Electrosynthesis under Ambient Conditions

Bryan H. R. Suryanto,¹ Colin S. M. Kang,¹ Dabin Wang,¹ Changlong Xiao,¹ Fengling Zhou,¹ Luis Miguel Azofra,² Luigi Cavallo,² Xinyi Zhang,¹ and Douglas R. MacFarlane^{1}*

¹School of Chemistry, Monash University, Clayton, VIC 3800, Australia

²KAUST Catalysis Centre (KCC), King Abdullah University of Science and Technology, Thuwal 23955-6900, Kingdom of Saudi Arabia

Corresponding Author

*E-mail: douglas.macfarlane@monash.edu

Table of Contents

1. Experimental
2. SEM-XRD Characterizations
3. Electrochemical cell, physicochemical and electrochemical properties of electrolyte systems
4. Electrochemical and X_{IL} optimization for NRR
5. List of the performed control NRR experiments
6. NRR performance of Fe₂O₃ nanorods
7. Supplementary figures
8. Electrochemically active surface area (ECSA) measurements
9. List of previously reported FE and yield rate of NRR catalyst at RTP
10. Computational details

1. Experimental:

Materials. 1-butyl-1-methylpyrrolidinium tris(pentafluoroethyl)trifluorophosphate ([C₄mpyr][eFAP]) was purchased from Merck (purity \geq 99.0%). Hydrofluoroether, 1H,1H,5H-octafluoropentyl 1,1,2,2-tetrafluoroethyl ether (FPEE) was purchased from Synquest. Anhydrous iron(III) chloride was purchased from Sigma-Aldrich. Sodium sulphate was purchased from Ajax Finechem. Carbon fibre paper (CFP) was purchased from Fuel Cell Store. The gases used in this study (Argon and N₂) were supplied by Air Liquide. Ultra-high purity grade AlphagazTM (H₂O < 3 ppm; O₂ < 2 ppm; C_nH_m < 0.5 ppm) N₂ and Ar were used in all experiments.

Iron nanorods synthesis. Prior to the modification of CFP with Fe NR, CFP was treated overnight with a piranha solution (3:1 v/v, H₂SO₄:10%H₂O₂) to introduce oxygen functional groups important for metal nucleation. In a glass beaker, 0.95 g of the anhydrous FeCl₃ was dissolved in 70 mL of 0.5 M Na₂SO₄ using a magnetic stirrer for 5 minutes. The solution was transferred into a Teflon lined autoclave containing 3 cm \times 2 cm of the piranha treated CFP. The autoclave was sealed and kept at 160°C for 6 hours. Following the hydrothermal reaction, a yellow film was formed (β -FeOOH) on the surface of the CFP. The film was rinsed thoroughly with Milli-Q water and ethanol and dried overnight in a vacuum oven at 60°C.

To synthesise the reduced α -Fe@Fe₃O₄, the β -FeOOH on CFP was annealed at 300°C for 2 hours, achieved with a ramping rate of 5°C min⁻¹ under a constant H₂ flow of 5 mL min⁻¹. Following the annealing, the initially yellow film was transformed into a black film and exhibited a strong ferromagnetism. The loading of the α -Fe NR on CFP was determined to be 0.5 mg cm⁻². For the synthesis of Fe₂O₃ NR, the β -FeOOH on CFP was annealed at 600°C for 2 hours.

Electrode preparation method: Prior to the surface functionalisation, CFP was treated with piranha solution to create surface-bound oxygen functionalities, important for the initial heteronucleation step of the metal cations. In a typical synthesis, 0.95 g of anhydrous FeCl_3 is dissolved in 70 mL of 0.5 M Na_2SO_4 . The mixture was transferred into a 100 mL Teflon-lined autoclave and hydrothermally treated at 160°C for 6 hours. Following the hydrothermal reaction, a uniform layer of bright-yellow $\beta\text{-FeOOH}$ coating was formed, as confirmed by X-ray diffraction (XRD) analysis shown in Figure 1.

Electrochemical cell set-up: Three electrode electrochemical cell comprised a working electrode (W.E., CFP@Fe NR), reference electrode (R.E.) and counter electrode (C.E., Pt wire) were used. To prepare the R.E., silver trifluoromethanesulfonate was dissolved in $[\text{C}_4\text{mpyr}][\text{eFAP}]$ to form a 10 mM Ag^+ electrolyte. The reference electrode was calibrated against normal hydrogen electrode (NHE) with ferrocene/ferrocenium couple (Fc/Fc^+) in $X_{IL} = 0.23$ electrolyte mixture (Figure S5), with a basis of $E^o(\text{Fc}/\text{Fc}^+) = 0.64 \text{ V vs. NHE}$. The C.E. used in this experiment is separated using a glass fritted anode chamber filled with the corresponding electrolyte. The electrochemical cell was sealed to prevent gas leakage. To prevent the re-oxidation of the produced ammonia, the Pt-wire counter electrode was isolated in a glass fritted compartment. Nitrogen gas and H_2O were supplied into the cell via Teflon tubing which was positioned close to the working electrode; the reacted gas is then passed into a 3 mL acid trap (1 mM H_2SO_4) to capture the produced NH_3 .

Electrochemical potential window determination method: Both the anodic and cathodic limits of the electrolytes were determined using baseline-faradaic currents profile intercept method.

Gas purification and treatment and NRR set-up: Gases used in this study (unless specifically mentioned) is further purified from NO_x, O₂ and H₂O by passing the gas through a 10 mM H₂SO₄ – Milli-Q trap, O₂ trap column (Agilent) and a H₂O trap column (Agilent), respectively. The flows of the wet and dry N₂ gas were regulated with separate gas flow meters to achieve various total water contents. Before entering the electrochemical cell, the gases were mixed in a mixing chamber. The reacted N₂ was then passed through a final 3 mL, 1 mM H₂SO₄ ammonia trap to capture the ammonia formed during the NRR.

Ammonia detection by the indophenol blue method: Ammonia was extracted from the reaction vessel containing the hydrophobic electrolyte mixture using 1 mL of Milli-Q washing solution. From the wash solution, 0.5 mL of Milli-Q was taken and transferred into a 1 mL sample tube. Into the tube 0.5 mL of 0.5 M NaClO₄, 50 μL of 1 M NaOH solution (with 5 wt.% salicylic acid and 5 wt.% sodium citrate) and 10 μL of 0.5 wt.% C₅FeN₆Na₂O (sodium nitroferricyanide) in water. The mixture was then incubated in the dark at room temperature for 3 hours before the UV-Vis test. The solution from the acid trap was also tested using the same procedure.

The concentration of ammonia is determined by a calibration plot (Figure S6). The calibration plot was prepared by dissolving a known amount of NH₄Cl in Milli-Q water. Subsequently the solutions were reacted with the indophenol blue method reagents and the ammonia content was determined using UV-Vis. The calibration plot was collected three times and the limit of detection (LOD) was determined to be 3 μM. Calibration plot for the 1 mM H₂SO₄ traps were also collected separately according to the described method (*vide supra*).

Faradaic efficiency (FE%) calculations. Faradaic efficiency was back-calculated from the amount of NH₃ detected by UV-Vis measurements (n_{UV-Vis}). The efficiency was determined by calculating the theoretical amount of produced NH₃ based on the six-electron transfer

process of dinitrogen reduction to ammonia using H₂O as proton source ($\text{N}_2 + 6 \text{H}_2\text{O} + 6 \text{e}^- \rightleftharpoons 2 \text{NH}_3 + 6 \text{OH}^-$), using the Faraday's law:

$$n_t = q / F z$$

Where:

n_t is the theoretical moles amount of produced ammonia.

q is the total electric charge passed for the duration of electrolysis (C).

F is the Faraday's constant (96485.3 C mol⁻¹).

z is the number of electron transfer involved in reduction of N atom (3 e⁻ per mole of NH₃).

Therefore, FE (%) is determined as follow:

$$\text{FE (\%)} = n_{UV-vis} / n_t \times 100\%$$

XRD measurements. Performed Bruker D8 Advance diffractometer instrument equipped with standard Cu anode, K- α wavelength = 1.54 nm. The typical scan range was 10° to 80°, collected with step size of 0.039° s⁻¹.

Scanning electron microscopy. SEM analysis were carried out with FEI Nova NanoSEM 450 FEGSEM with a 10 kV accelerating voltage.

Transmission electron microscopy. TEM was carried out with FEI Tecnai G2 F20 microscope. To prepare TEM samples, the CFP supported catalyst was transferred to Cu-grid by physically scratching the electrode using a sharp knife. The resulting powder was dispersed in absolute ethanol by ultrasonication for 15 mins. The resulting mixture was then drop-casted onto Cu-grid and dried in room temperature.

2. SEM-XRD Characterizations

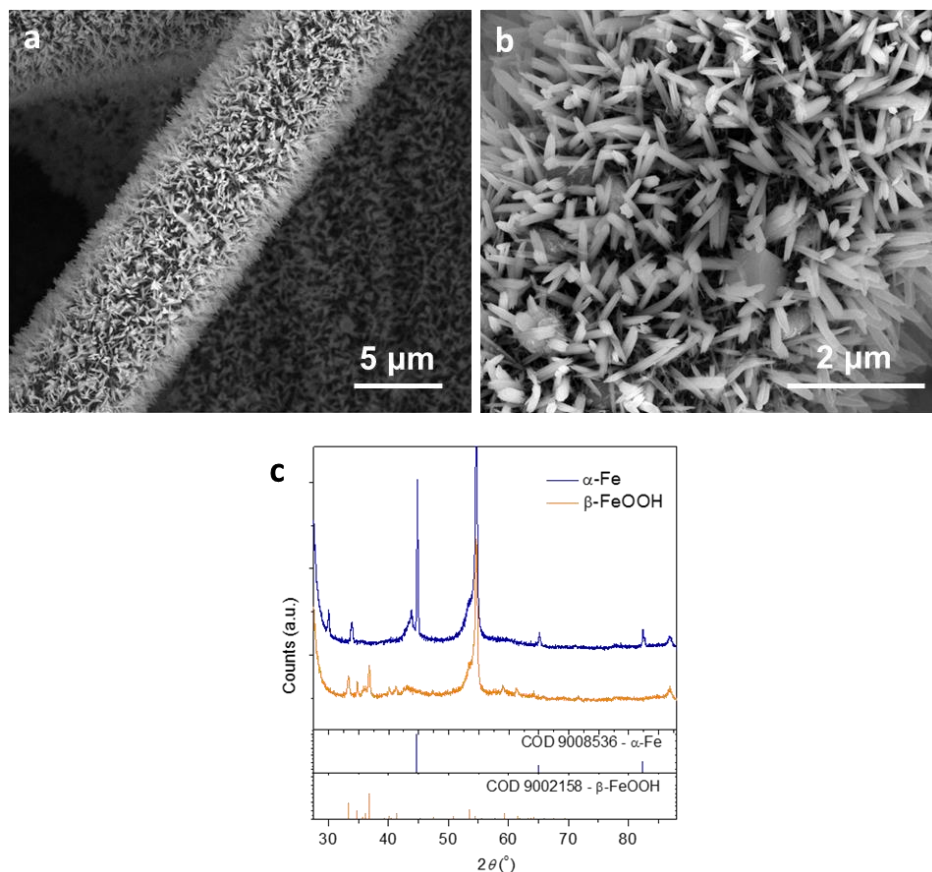


Figure S1. (a-b) Scanning electron microscopy (SEM) of β -FeOOH; (c) X-ray diffraction (XRD) characterisation of the synthesised Fe nanorods on CFP.

Thermal annealing under H_2 -atmosphere was employed to reduce the as-synthesised β -FeOOH into α -Fe. The successful synthesis of α -Fe was validated by both X-ray diffraction (XRD) and scanning electron microscopy characterisation techniques. XRD reveals the presence of an intense α -Fe peak at 44.8° , that arises from (110) crystal plane in the α -Fe body centred cubic (bcc) system with $Im-3m$ space group (COD 9008536).¹ In addition, relatively weaker peaks observed at 30.0° , 33.8° and 43.7° correspond to the (220), (311) and (400) crystal planes in Fe_3O_4 . The presence of Fe_3O_4 can be attributed to the formation of a

passivating oxide layer from atmospheric exposure of Fe to oxygen.² We refer to this Fe₃O₄ coated iron as α -Fe@Fe₃O₄.

3. Electrochemical Cell, Physicochemical and Electrochemical Properties of Electrolyte Systems

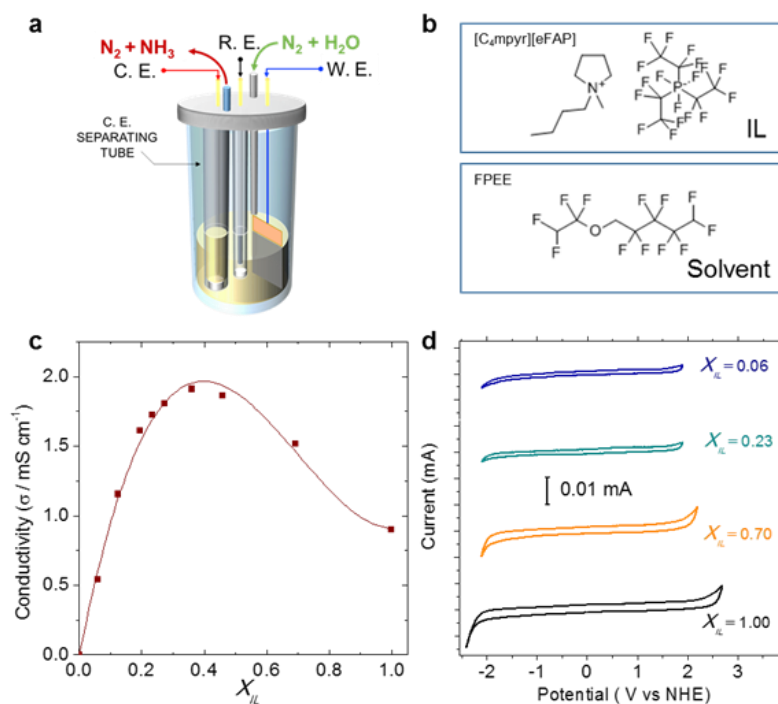


Figure S2. (a) Schematic of the NRR electrochemical cell used in this study (C.E. – counter electrode; R.E. – reference electrode, W.E. – working electrode); (b) Structure of the IL and solvent; (c) Conductivity dependence on [C₄mpyr][eFAP] mol fraction (X_{IL}) in FPEE; (d) Electrochemical potential window comparisons of [C₄mpyr][eFAP] and FPEE/[C₄mpyr][eFAP] mixtures with various X_{IL} on glassy carbon electrode.

In designing the electrolyte for this work, we observed that [C₄mpyr][eFAP] was not miscible with some solvents (*e.g.*, perfluoromethyldecalin and perfluorohexane), therefore, 1*H*,1*H*,5*H*-octafluoropentyl 1,1,2,2-tetrafluoroethyl ether (FPEE) was chosen due to its high degree of fluorination and high miscibility with [C₄mpyr][eFAP] (Figure S2b). The physicochemical and electrochemical properties of FPEE, [C₄mpyr][eFAP], and their

mixtures were initially characterised to determine the optimum solvent – IL ratio for electrochemical measurements. As displayed in the plot of conductance vs. IL mole fraction (X_{IL}) in FPEE in Figure S2c, a maximum conductivity of 1.95 mS cm^{-1} is achieved with X_{IL} of ~ 0.4 . The cyclic voltammograms (CVs) in Fig S2d show the effect of FPEE content on the potential window of the electrolyte. As shown in Figure S2d, the mixtures exhibit cathodic limit of at least -1.90 V vs. NHE and an anodic limit beyond 1.5 V (Table S2 for full details). Hence, the results indicate the suitability of FPEE as an electrolyte system for NRR.

4. Electrochemical and X_{IL} optimization for NRR

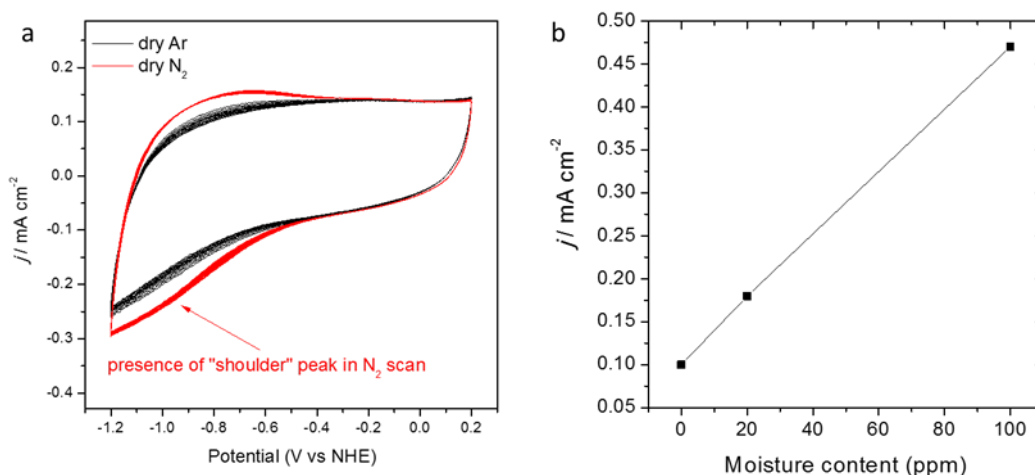


Figure S3. (a) Comparison of multiple cyclic voltammeteries indicating steady state; (b) Comparison of the anodic currents collected in Ar with different moisture concentration.

Nitrogen gas feedstock with a controlled amount of moisture ($C_{H_2O} = \sim 100 \text{ ppm}$) was used as proton source for the formation of NH_3 . Prior to CPE experiments, the $\alpha\text{-Fe@Fe}_3\text{O}_4$ NR cathodes were subjected to electrochemical activation at -1.35 V vs. NHE for 60 s to remove the passivating oxide layers. During this period, only $\sim 0.2 \text{ nmol NH}_3$ was detected, which is insignificant compared to the average yields reported herein (10 – 30 nmols) in our main experiments.

5. List of the performed NRR control experiments:

Considering the possible presence of NH_3 (as detected with UV-Vis, unless otherwise stated) and NO_x in the used electrolytes, solutions, gas supplies and electrodes, the following control experiments have been carried out (results are shown in Table S1):

- Control No. 1: Determination of ammonia amount in the Milli-Q water.** The measurement revealed NH_3 amount below LOD.
- Control No. 2: Determination of ammonia amount in the 1 mM H_2SO_4 trap solution.** The measurement revealed NH_3 amount below LOD.
- Control No. 3: Determination of ammonia/ NO_x amount in N_2 feedstock.** The measurement was carried out using a flow injection analysis (FIA). 18 L of N_2 was passed through 1 ml of Milli-Q water. The measurement revealed both NO_x and NH_3 amounts of less than LOD of FIA method (1 nmol ml^{-1}).
- Control No. 4: Determination of ammonia amount in the used electrochemical cell containing electrolytes and electrodes (no potential applied).** The measurement revealed the NH_3 amount was very close to LOD of 3 nmols.
- Control No. 5: Determination of ammonia amount in the used electrochemical cell containing electrolytes and electrodes (under Argon, applied potential of -0.65 V vs NHE).** The measurement revealed NH_3 amount was very close to LOD of 3 nmols, *This experiment has indicated that without N_2 , NH_3 was not generated.*

Table S1. List of the performed control and background determination experiments, the gases used in these experiments contained 106 ± 5.0 ppm moisture. In all experiments, 1 ml of test solution was quantified. Therefore 1 μM detected is equivalent to 1 nmol of NH_3 in the test solution.

Control No.	Electrode	Solutions/Electrolyte	Gas	Time / E (V)	NH_3 detected (μM)
1		Milli-Q		No Applied potential	below LOD
2		1 mM H_2SO_4 trap		No Applied potential	below LOD
3*		Milli-Q	N_2 (flow rate: 100 ml min^{-1})	3 h (18 L)/ No Applied potential	below FIA LOD
4	$\alpha\text{-Fe NR@Fe}_3\text{O}_4$	$X_{\text{IL}} = 0.23$ mixture	N_2	3 h / No Applied potential	3.0
5	$\alpha\text{-Fe NR@Fe}_3\text{O}_4$	$X_{\text{IL}} = 0.23$ mixture	Ar	3 h / -0.65 V vs NHE	3.0

*Result was obtained by liquid chromatography-flame ionisation analysis.

6. NRR Performance of Fe₂O₃ nanorods

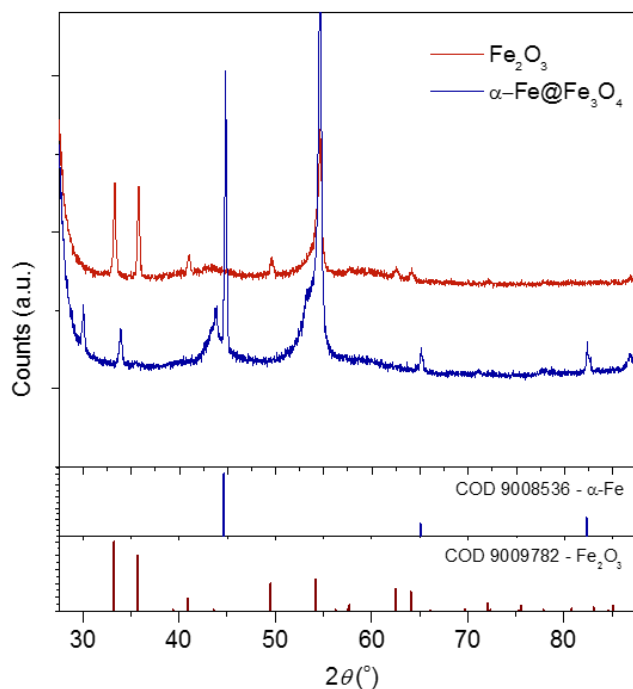


Figure S4. XRD patterns comparison of α-Fe@Fe₃O₄ with the fully oxidised Fe₂O₃.

We also attempted to experimentally determine the nature of the electrocatalytically active Fe centres for NRR. A fully oxidised Fe₂O₃ NR control electrode was derived by gradually oxidising α-Fe@Fe₃O₄ NR core-shell structure in the presence of O₂. The oxidation was validated by XRD characterisations of Fe₂O₃ as shown in Figure S4, showing that the peak at $2\theta = 45^\circ$ for α-Fe (110) has disappeared. Although at the optimised potential of -0.65 V Fe₂O₃ NR cathode exhibits higher cathodic j , the NRR activity was significantly lower. The NH₃ was formed with FE of < 1.00% and a yield rate of $< 0.5 \times 10^{-11} \text{ mol s}^{-1} \text{ cm}^{-2}$. Therefore, in contrast to previous reports on NRR in aqueous media,³⁻⁵ there is a strong indication that

Fe₂O₃ is not the catalytically active centre for NRR in our electrolyte system, rather it is the metallic/reduced Fe-species.

7. Supplementary figures and data

Table S2. Electrochemical potential windows of [C₄mpyr][eFAP] and the mixed electrolytes collected under inert Ar atmosphere.

X_{IL}	Cathodic Limit (E_c)*	Anodic Limit (E_a)*	ΔE (V)
0.06	-1.9	1.5	3.4
0.23	-1.9	1.6	3.5
0.7	-2	1.9	3.9
1	-2.2	2.4	4.6

*The quoted potentials are calibrated against NHE.

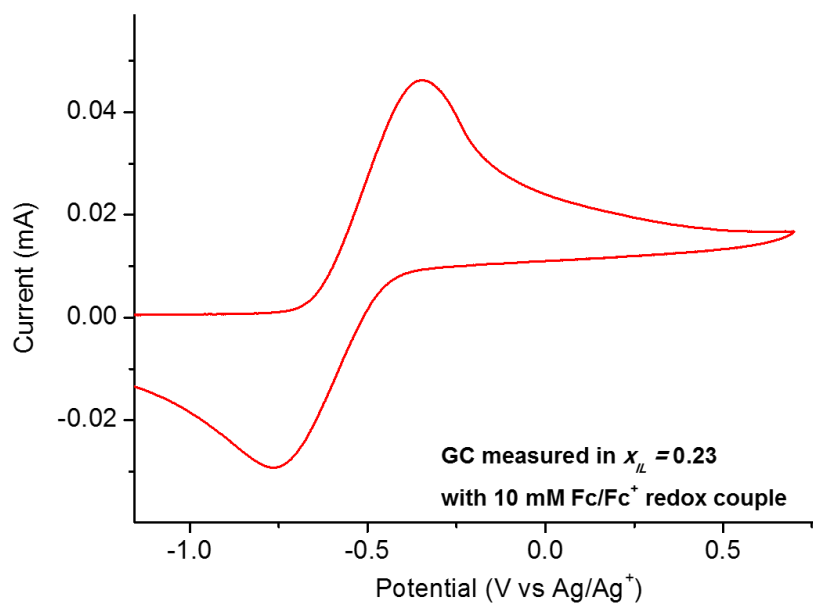


Figure S5. Cyclic voltammetry of the Fc/Fc⁺ in $X_{IL} = 0.23$ electrolyte mixture to calibrate the Ag/Ag⁺ reference electrode.

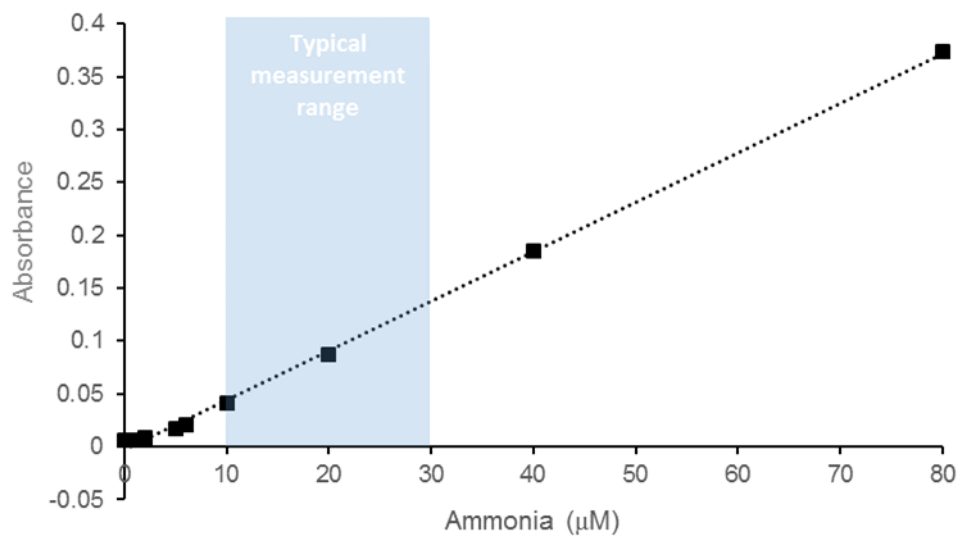


Figure S6. Ammonia – indophenol calibration plot used in this study. The area shaded in blue indicates the typical range in which ammonia was produced in this study.

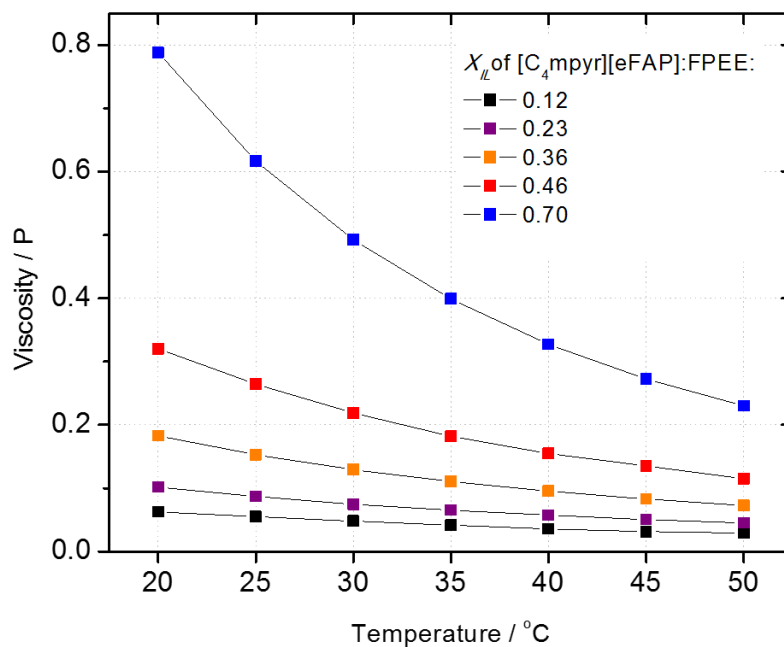


Figure S7. Viscosity profile of different electrolyte mixtures as a function of temperature.

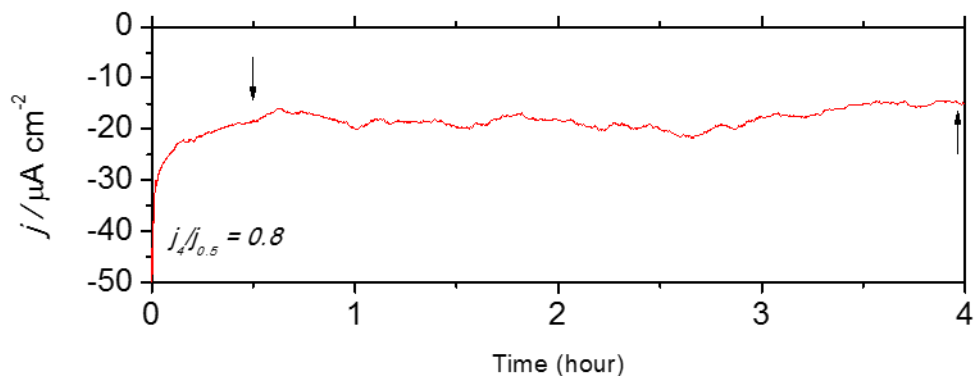


Figure S8. Controlled potential electrolysis stability testing at an applied potential of -0.65 V vs NHE for 4 hours (moisture level = 100 ppm).

Table S3. Effect of moisture concentration in electrolyte mixture ($X_{IL} = 0.23$) on NRR activity. (Data is mean and std dev of $n = 3$ repeats unless otherwise noted).

Moisture concentration (ppm) ^a	NH ₃ Yield Rate ($\times 10^{-11}$ mol s ⁻¹ cm ⁻²)	Faradaic Eff. (%)
1.1 ± 1.0	0.28*	0.8*
50 ± 17	0.82 ± 0.22	8.5 ± 0.3
106 ± 5.0	1.58 ± 0.05	23.8 ± 0.8
114.3 ± 5.7	2.15 ± 0.20	30.8 ± 1.6
144.3 ± 4.8	0.95*	17*
186.2 ± 8.3	0.60*	9.9*

*No repeats

^a The moisture concentrations were determined using Karl-Fischer titration method.

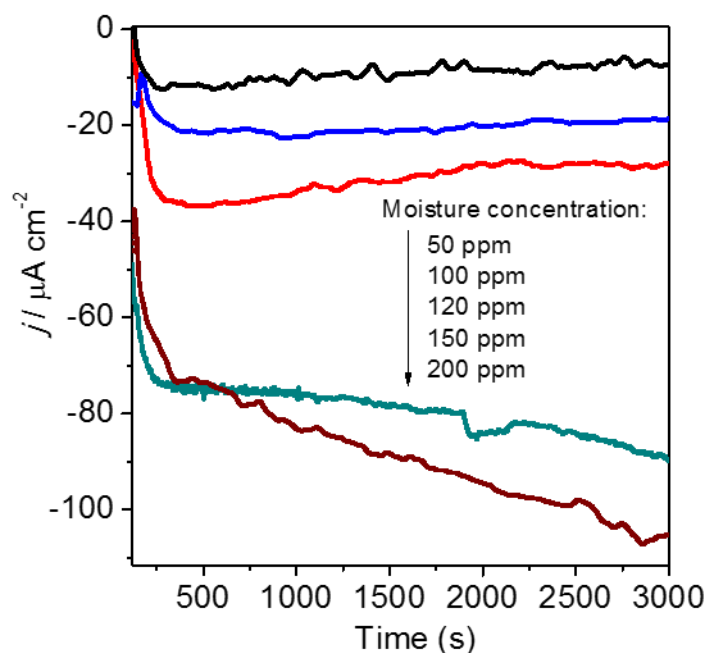


Figure S9. Controlled potential electrolysis testing revealing the effect of moisture concentration in the total electrolysis current density at an applied potential of -0.65 V. (CPE was collected under static conditions, electrolyte was initially saturated with N_2 and known amount of H_2O was added).

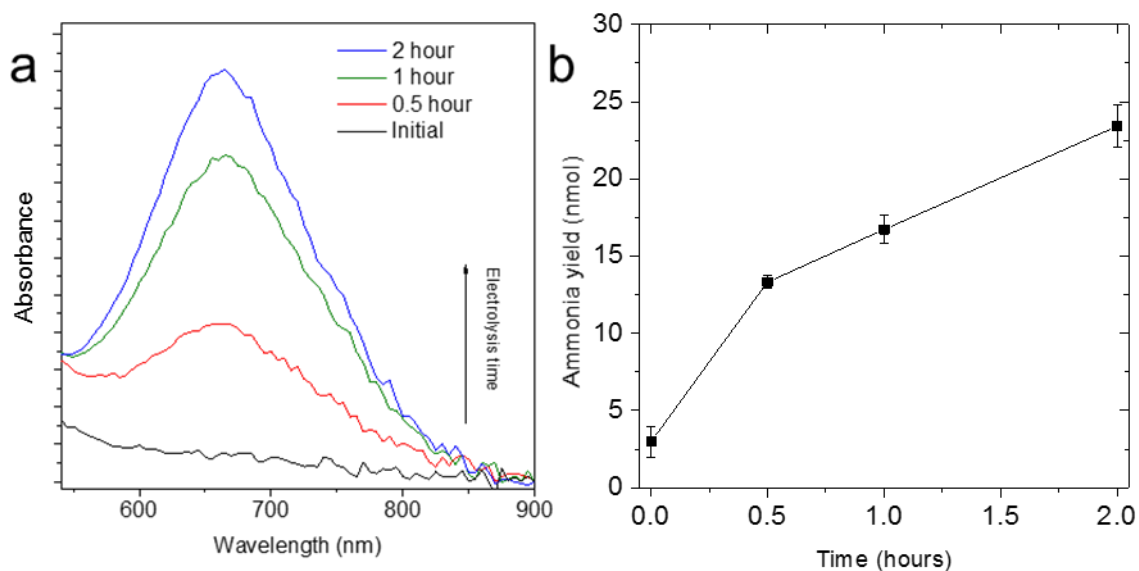


Figure S10. Time dependent NH_3 formation from NRR in the optimised conditions: (a) The indophenol UV-Vis response for different electrolysis times; (b) the corresponding plot of the total ammonia yield vs. time.

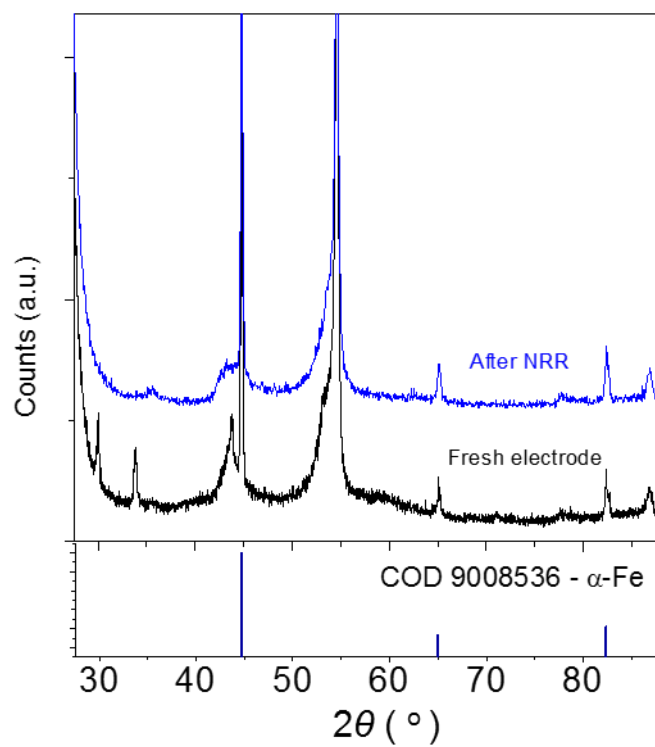


Figure S11. XRD characterizations comparing the spectra of fresh α -Fe@Fe₃O₄ NR and post-NRR electrode.

8. Electrochemically active surface area (ECSA) measurements

The electrochemically active surface area of α -Fe/Fe₃O₄ was determined by double-layer capacitance measurements (Fig S12). To determine the electrochemically active surface area (ECSA), general specific capacitance (C_s) for nanostructured metal oxides of 0.040 mF cm⁻² was used,⁶ and ECSA was calculated according to standard method.⁶ ECSA value of 47.5 cm² was obtained from an electrode with geometric surface area (GSA) of 0.75 cm².

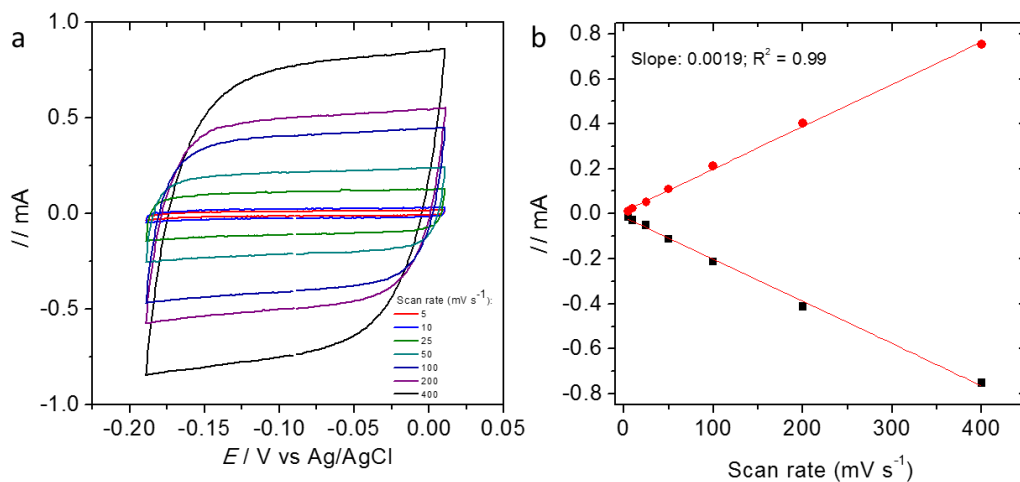


Figure S12. (a) Double-layer capacitance measurements by cyclic voltammetric scan at various scan rates (ν) ranging from 5 – 400 mV s⁻¹. (b) I - ν plot for the measurement of C_{dl} .

Table S4. ECSA normalised NH₃ yield rate

X_{IL}	Yield rate (GSA) (mol s ⁻¹ cm ⁻²)	Yield rate (ECSA) (mol s ⁻¹ cm ⁻²)
0.12	6.57×10^{-12}	1.04×10^{-13}
0.16	7.82×10^{-12}	1.24×10^{-13}
0.2	5.96×10^{-12}	9.41×10^{-14}
0.23	1.59×10^{-11}	2.51×10^{-13}
0.24	5.52×10^{-12}	8.72×10^{-14}
0.46	2.78×10^{-12}	4.39×10^{-14}

9. List of previously reported FE and yield of NRR catalysts at RTP

Table S5. List of previously reported FE and yields of NRR catalysts at RTP

Cathode	Electrolyte	Anode	Yield rate (mol cm ⁻² s ⁻¹)	FE (%)	J_{NRR}^{**} ($\mu\text{A cm}^{-2}$)	Potential (vs NHE)*	<i>T</i>	Year	Ref.
Fe electrode	6N KOH	Stainless Steel	0.6×10^{-14}	Not reported	n.a.	-0.85 V	25	1983	[7]
Ru/C	Nafion	Pt	3.43×10^{-12}	0.28%	n.a.	-0.9 V	25	2000	[8]
Pt/Ppy (polypyrrolle)	Li ⁺ /H ⁺	Pt/C	3.61×10^{-11}	< 0.1%	n.a.	-0.165 V	25/60 bar	2010	[9]
Pt/C	Nafion	Pt	1.14×10^{-9}	0.55%	1050 ^a	0.2 V vs RHE	25	2013	[10]
Porous Ni	H ₂ SO ₄ /2-Propanol	Pt	1.75×10^{-11}	0.90%	4.75	3.5 V bias	25	2016	[11]
Fe/CNT	Nafion/GDL	Pt	3.59×10^{-12}	0.03%	1.2	-2.0 V	25	2016	[12]
Au NR	0.1 M KOH/Nafion	Pt	2.69×10^{-11}	4.00%	10	-0.2 V	25	2016	[13]
Au/TiO ₂	HCl/Nafion	Pt	5.94×10^{-9}	8.11%	35	-0.2 V vs RHE	25	2017	[14]
Au-CeOx/RGO	HCl/Nafion	Pt	1.35×10^{-10}	10.10%	10	-0.2 V vs RHE	25	2017	[15]
Polyimide/C	Li ⁺ /H ⁺	Pt	7.68×10^{-12}	2.91%	<10	-0.4 V vs RHE	25	2017	[16]
Fe electrode/FTO	[P _{6,6,6,14}][eFAP]	Pt	4.7×10^{-12}	60.00%	0.72	-0.8 V	25	2017	[17]
Mo Nanofilm	0.01 M H ₂ SO ₄	Pt	3.09×10^{-11}	0.72%	5.5	-0.39 V vs RHE	25	2017	[18]
γ -Fe ₂ O ₃	0.1 M KOH	Pt	1.20×10^{-11}	2.0%	4	0.0 V vs RHE	25	2017	[19]
Polyaniline@Pt	H ₂ SO ₄ /LiClO ₄ /MeOH	Pt	4.8×10^{-12}	1.3%	0.91 ^b	-0.12 V	25	2006	[20]
α-Fe@Fe₃O₄	[C₄mpyr][eFAP]-FPEE mix	Pt	2.35×10^{-11}	32.0%	12	-0.6 V	25	2017	This work

*Ag/AgCl was converted to NHE on the basis of $E(\text{Ag}/\text{AgCl}) = 0.197 \text{ V vs. NHE}$; SCE was converted to NHE on the basis of $E(\text{SCE}) = 0.240 \text{ V vs. NHE}$.

** J_{NRR} = practical NRR current ($j_{\text{operational}} \times \text{NRR FE}$); ^aindustrial-grade cell, air as N₂ source and H₂ used as proton source; ^bcalculated based on reported average current.

10. Computational details

The mechanism for N₂ adsorption and its further electrochemical conversion into NH₃ catalysed by α -Fe(110) has been studied by means of density functional theory (DFT) through the generalised gradient approximation (GGA) with the revised Perdew-Burke-Ernzerhof (RPBE) functional with Pade approximation,²¹ using a plane-wave cut-off energy of 400 eV.^{22,23} The Brillouin zone (periodic boundary conditions) was sampled by 5×5×1 k -points using the Monkhorst-Pack scheme. In order to avoid interactions between periodic images, a vacuum distance of 17 Å was imposed between different layers. Optimisation calculations were done using energy and force convergence limits equal to 10⁻⁴ eV/atom and |0.01| eV/Å, respectively. Due to the paramagnetic properties of the α -Fe catalyst, spin-polarised calculations were imposed in all cases. Over these optimised structures, vibrational frequencies were calculated over Γ points in order to obtain zero-point energies (ZPE), thermal corrections and entropy contributions. At this step, explicit dispersion correction terms to the energy were also employed through the use of the D3 method with the standard parameters programmed by Grimme and co-workers.^{24,25} All optimisation and vibrational frequency calculations have been performed throughout the facilities provided by the Vienna *Ab-Initio* Simulation Package (VASP, version 5.4.1).²⁶⁻²⁹

10.1. DFT characterisation of the α -Fe(110) catalyst

Experimental crystal structure of bcc Fe (α -Fe) unit cell was taken and treated with Materials Studio. According to XRD characterisation of the material (see Figure S1), the unit cell was expanded and truncated to conform a slab of 80 Fe atoms (Fe₈₀) constituted by five layers or 16 Fe atoms each one and being terminated with a (110) surface.

Due to the paramagnetic properties of α -Fe(110) catalyst, spin-polarised considerations were imposed during optimisation. Different magnetic moments for Fe atoms were tested in order to correctly define magnetisation, and therefore energetic properties of the material. At RPBE

functional, magnetic moments for Fe atoms have been calculated as 2.602, 2.365, 2.327, 2.365 and 2.602 μ , for the first, second, third, fourth and fifth Fe layers, respectively. These parameters have been used as initial magnetic moments for Fe atoms during the NRR modelling ($\mu = 0$ for N and H atoms).

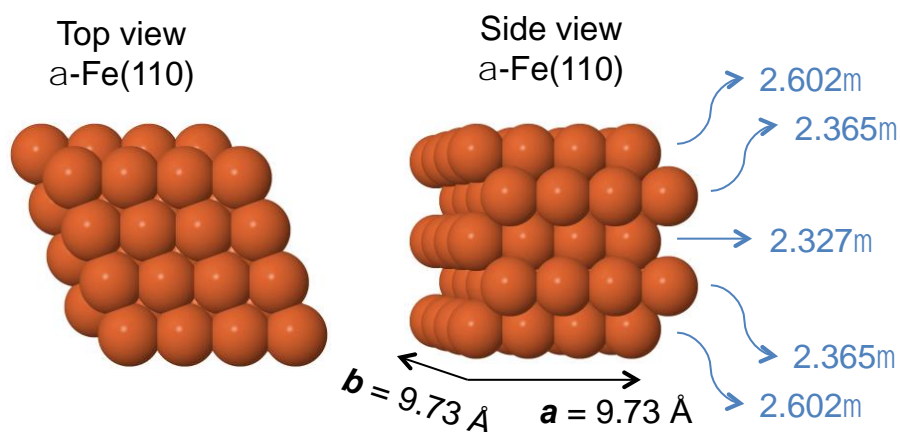
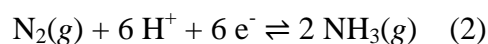


Figure S13. Top and side views of α -Fe₈₀(110) slab and optimised lattice parameters and magnetic moments at RPBE functional

10.2. Modelling performance

Once α -Fe₈₀(110) slab is properly optimised, NRR mechanism was investigated by optimising the different states during N₂ conversion when interacting on the flat (110) surface. All Fe atoms of this (110) surface are equivalent.

Once N₂ is adsorbed on the catalytic surface (*N₂), a set of six H⁺/e⁻ pair transfers occur; the first leading to *N₂H, the second to *NHNH or *NNH₂, and so on up to balance chemical Equation (2):



For all these states, the first three layers of Fe slab were frozen during optimisation (Figure S14), since it can be approximated that chemical events taking place on the surface do not affect to atoms from inner layers.

Over these optimised geometries, vibrational frequencies were calculated in order to obtain zero-point energies (ZPE), thermal corrections and entropy contributions. In such cases, all Fe atoms were frozen during vibrational frequency calculations, imposing no constraints for N and H atoms. At this stage, explicit D3 dispersion corrections were also applied

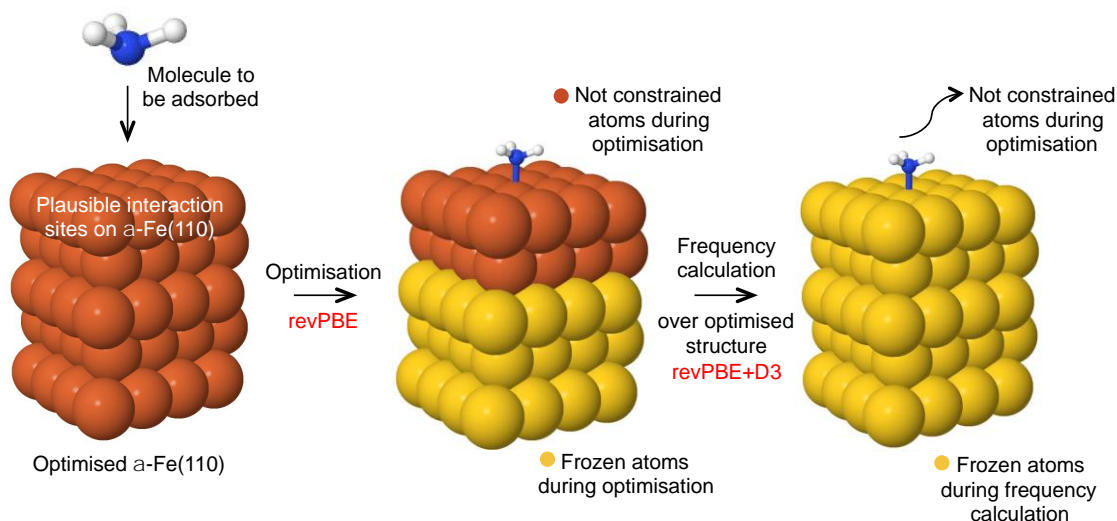


Figure S14. Modelling performance for optimisation and frequency calculations.

10.3. Thermochemistry

DFT calculations have been performed using revised PBE (RPBE) functional, which offers a better estimation of the reaction energy for hydrogenation of N_2 into ammonia than classical PBE: -0.50 eV (RPBE) *vs.* -0.34 eV (experimental).

Gibbs free energy calculation has been carried out as it follows:

$$\mu = E + \int C_p dT - TS \quad (3)$$

where μ , E and C_p refer to the chemical potential (partial molar Gibbs free energy), electronic energy and heat capacity, respectively.

The entropy term can be expressed as the sum of the translational, rotational, vibrational and electronic contributions as to:

$$S = S_t + S_r + S_v + S_e \quad (4)$$

And finally, intrinsic zero-point energy (ZPE) and extrinsic dispersion (D) corrections can be included to finally obtain:

$$\mu = E + \int C_P dT - T(S_t + S_r + S_v + S_e) + \text{ZPE} + D \quad (5)$$

Since $S_e \approx 0$ at the fundamental electronic level, Table S6 gathers the thermodynamic quantities for N_2 , H_2 and NH_3 gases at standard condition (298.15K of temperature, 1 bar of fugacity for all gases).

Table S6. Thermodynamic quantities, in eV, for N_2 , H_2 and NH_3 gases at standard condition (298.15K, $f = 1$ bar) using RPBE functional.

Gas	$E(+D)$	$\int C_P dT$	$-TS$	ZPE	D
$\text{N}_2(g)$	-16.24	0.09	-0.59	0.15	-16.60
$\text{H}_2(g)$	-6.98	0.09	-0.40	0.27	-7.02
$\text{NH}_3(g)$	-19.47	0.11	-0.62	0.91	-19.08

For the case of solids and adsorbates, some approximations can be assumed:

1. As for gases, at the fundamental electronic level $S_e \approx 0$.
2. Translational and rotational motions can be neglected, therefore, $S_t \approx 0$ and $S_r \approx 0$. In this sense, all entropy contributions comes from vibrations: $S = S_v$. Similarly, translational and rotational contributions to the heat capacity are neglected.

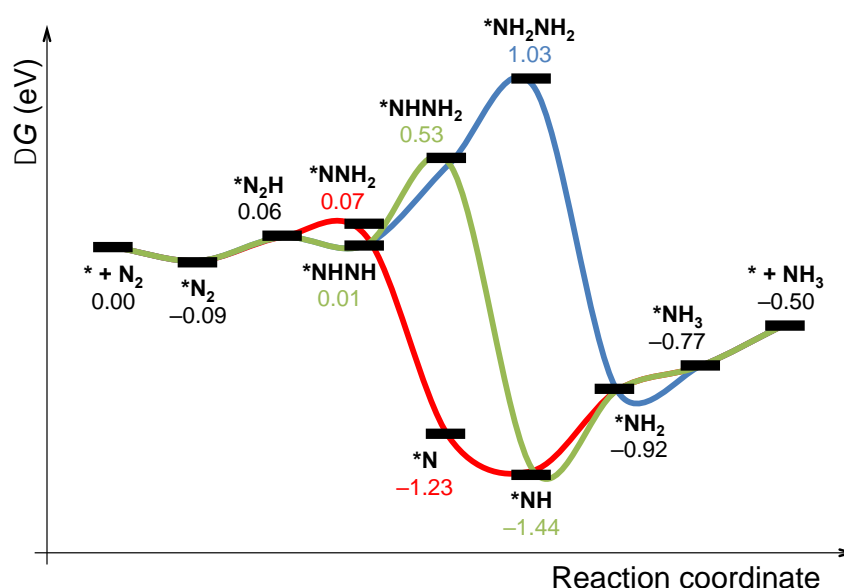
Equation. (5) results in:

$$G = E + \int C_P dT - TS_v + \text{ZPE} + D \quad (5)$$

Therefore, Gibbs free energies for the different states along NRR have been calculated as to:

Table S7. Gibbs free energies, in eV, for the different states along NRR mechanism at standard condition (298.15K) using RPBE functional. (Attached, relative Gibbs free energy diagram, with the minimum energy path indicated in green).

State	G	State	G	State	G
*	0.00	*NHNH	0.01	*NH	-1.44
*N ₂	-0.09	*NNH ₂	0.07	*NH ₂ NH ₂	1.03
*N ₂ H	0.06	*N	-1.23	*NH ₂	-0.92
		*NHNH ₂	0.53	*NH ₃	-0.77



10.4. Proton-coupled electron transfer (PCET) approach

The reaction Gibbs free energy between two states along the N₂ capture/conversion process carried out *via* electrochemical approach, *i.e.*, $\text{N}_2(\text{g}) + 6 \text{H}^+ + 6 \text{e}^-(\text{aq}) \rightleftharpoons 2 \text{NH}_3(\text{g})$, can be expressed, by applying the proton-coupled electron transfer (PCET) approach,³⁰ as to:

$$\Delta G_{\text{R}} = G(*\text{N}_{2-m}\text{H}_n) + mG(\text{NH}_3) - G(*) - G(\text{N}_2) - nG(\text{H}^+/\text{e}^-) \quad (6)$$

where ‘*’ denotes the surface material, n is the number of H^+/e^- pairs transferred and m the number of NH_3 molecules released, if applicable ($m = 0, 1$). Obviously, for $n = m = 0$, the reaction Gibbs free energy leads to the binding Gibbs free energy:

$$\Delta G_b = G(*N_2) - G(*) - G(N_2) \quad (6.1)$$

In this regard, all energy values have been referred using the computational hydrogen electrode (CHE) model for the H^+/e^- transfer, considering the chemical potential of the H^+/e^- pair in aqueous solution as the half of the H_2 gas molecule at standard hydrogen electrode (SHE) condition, *i.e.*, $f(H_2) = 1$ bar, $U = 0$ V and $pH = 0$, being $f(H_2)$ and U the fugacity of H_2 and the external potential applied, respectively.

$$\mu(H^+/e^-) = \frac{1}{2} \mu(H_2) \quad (7)$$

And therefore, Equation. (6) can be expressed as to:

$$\Delta G_R = G(*N_{2-m}H_n) + mG(NH_3) - G(*) - G(N_2) - n/2 G(H_2) \quad (6)$$

Supplementary references:

- (1) Vayssieres, L.; Rabenberg, L.; Manthiram, A., *Nano lett.* **2002**, *2*, 1393-1395.
- (2) Konishi, H.; Yamashita, M.; Uchida, H.; Mizuki, J. i., *Mater. trans.* **2005**, *46*, 329-336.
- (3) Kong, J.; Lim, A.; Yoon, C.; Jang, J. H.; Ham, H. C.; Han, J.; Nam, S.; Kim, D.; Sung, Y.-E.; Choi, J.; Park, H. S., *ACS Sus. Chem. Eng.* **2017**, *5*, 10986-10995.
- (4) Cui, B.; Zhang, J.; Liu, S.; Liu, X.; Xiang, W.; Liu, L.; Xin, H.; Lefler, M. J.; Licht, S., *Green Chem.* **2017**, *19*, 298-304.
- (5) Licht, S.; Cui, B.; Wang, B.; Li, F.-F.; Lau, J.; Liu, S., *Science* **2014**, *345* (6197), 637-640.
- (6) C. C. L. McCrory, S. Jung, J. C. Peters, T. F. Jaramillo, *J. Am. Chem. Soc.* **2013**, *135*, 16977-16987.
- (7) A. Scalfani, V. Augugliaro, M. Schiavello, *J. Electrochem. Soc.* **1983**, *130*, 734.
- (8) V. Kordali, G. Kyriacou, C. Lambrou, *Chem. Commun.* **2000**, 1673.
- (9) F. Köleli, D. B. Kayan, *J. Electroanal. Chem.* **2010**, *638*, 119.
- (10) R. Lan, J. T. S. Irvine, S. Tao, *Sci. Rep.* **2013**, *3*, 1145.
- (11) K. Kim, N. Lee, C.-Y. Yoo, J.-N. Kim, H. C. Yoon, J.-I. Han, *J. Electrochem. Soc.* **2016**, *163*, F610.
- (12) S. Chen, S. Perathoner, C. Ampelli, C. Mebrahtu, D. Su, G. Centi, *Angew. Chem. Int. Ed.* **2017**, *56*, 2699.
- (13) D. Bao, Q. Zhang, F.-L. Meng, H.-X. Zhong, M.-M. Shi, Y. Zhang, J.-M. Yan, Q. Jiang, X.-B. Zhang, *Adv. Mater.* **2017**, *29*, 1604799.

- (14) M.-M. Shi, D. Bao, B.-R. Wulan, Y.-H. Li, Y.-F. Zhang, J.-M. Yan, Q. Jiang, *Adv. Mater.* **2017**, *29*, 1606550.
- (15) S.-J. Li, D. Bao, M.-M. Shi, B.-R. Wulan, J.-M. Yan, Q. Jiang, *Adv. Mater.*, **2017**, *29*, 1700001.
- (16) G.-F. Chen, X. Cao, S. Wu, X. Zeng, L.-X. Ding, M. Zhu, H. Wang, *J. Am. Chem. Soc.* **2017**, *139*, 9771.
- (17) M. Ali, F. Zhou, K. Chen, C. Kotzur, C. Xiao, L. Bourgeois, X. Zhang, D. R. MacFarlane, *Nat. Commun.* **2016**, *7*, 11335.
- (18) D. Yang, T. Chen, Z. Wang, *J. Mater. Chem. A* **2017**, *5*, 18967.
- (19) J. Kong, A. Lim, C. Yoon, J. H. Jang, H. C. Ham, J. Han, S. Nam, D. Kim, Y.-E. Sung, J. Choi, H. S. Park, *ACS Sus. Chem. Eng.* **2017**, *5*, 10986.
- (20) F. Köleli, T. Röpke, *Appl. Catal. B Environ.* **2006**, *62*, 306
- (21) Hammer, B.; Hansen, L. B.; Nørskov, J. K., *Phys. Rev. B* **1999**, *59* (11), 7413-7421.
- (22) Blöchl, P. E., *Phys. Rev. B* **1994**, *50* (24), 17953-17979.
- (23) Kresse, G.; Joubert, D., *Phys. Rev. B* **1999**, *59* (3), 1758-1775.
- (24) Grimme, S.; Antony, J.; Ehrlich, S.; Krieg, H., *J. Chem. Phys.* **2010**, *132* (15), 154104.
- (25) Grimme, S.; Ehrlich, S.; Goerigk, L., *J. Comput. Chem.* **2011**, *32* (7), 1456-1465.
- (26) Kresse, G.; Hafner, J., *Phys. Rev. B* **1993**, *47* (1), 558-561.
- (27) Kresse, G.; Hafner, J., *Phys. Rev. B* **1994**, *49* (20), 14251-14269.
- (28) Kresse, G.; Furthmüller, J., *Phys. Rev. B* **1996**, *54* (16), 11169-11186.
- (29) Kresse, G.; Furthmüller, J., *Comput. Mater. Sci.* **1996**, *6* (1), 15-50.
- (30) Peterson, A. A.; Abild-Pedersen, F.; Studt, F.; Rossmeisl, J.; Nørskov, J. K., *Energy Environ. Sci.* **2010**, *3* (9), 1311-1315.